

Spontaneous emergence of run-and-tumble-like dynamics in coupled self-propelled robots: experiment and theory

Somnath Paramanick^{1,*}, Umashankar Pardhi^{2,*}, Harsh Soni^{2,†} and Nitin Kumar^{1,‡}

¹*Department of Physics,
Indian Institute of Technology Bombay Powai,
Mumbai 400076, India*

²*School of Physical Sciences,
Indian Institute of Technology Mandi, Mandi 175001, India*

(Dated: February 4, 2025)

Drawing inspiration from the motility behaviour of microorganisms, we introduce a highly tunable, robotic system self-actuating into the run-and-tumble (RT)-like motion. It comprises two disk-shaped, centimeter-scale programmable robots individually programmed to perform overdamped active Brownian (AB) motion and connected by a rigid rod. The rod is attached to pivot points located on off-centered, mirror-symmetric points on each robot, allowing for its free rotation at both ends. We show that the collective dynamics of this system execute RT-like motion with characteristic sharp tumble events and exponentially distributed run times, similar to those observed in microorganisms. We further quantify emerging dynamics in terms of tumbling frequency and tune it over a wide range of experimental parameters. We also develop a theoretical model that reproduces our experimental results and elucidates the underlying physical mechanisms governing the rich phase behavior of RT motion. Together, these results highlight the importance of our robotic platform in offering valuable insights into the mechanism of motility characteristics in microorganisms.

I. INTRODUCTION

Motility is one of the defining features of active and living organisms across all length scales [1–3]. One prominent example is run-and-tumble (RT) motion, a behavior commonly observed in swimming microorganisms living in a low Reynolds number environment [4–8]. As the name suggests, these organisms trace relatively straight paths (“runs”) before abruptly changing to a new, randomly chosen direction (“tumbles”). This type of motion is integral to key biological processes such as chemotaxis, nutrient foraging, escaping unfavorable environments, and colonization [9, 10]. Experimental investigations reveal that the RT motion originates through coordinated dynamics of multiple active units shaped as filamentous appendages, called flagella or cilia, decorating the body of microorganisms. These units exhibit intrinsic activity through their rhythmic beating, propelling the organism forward in a series of synchronous and asynchronous cycles [5, 11–18]. However, the precise mechanisms by which the collective motion of these active units produce motility remains an open question and a topic of active research.

Most organisms exhibiting RT motion lack cognitive abilities or centralized control systems like the brain. Therefore, simple coupling rules between its active components must govern their dynamics. Since run and tumble states are associated with translational and rotational motion, they likely originate from an interplay between

active forces and their corresponding moments respectively. Moreover, since they swim in a fluid medium, attempts have been made to investigate the effects of hydrodynamic coupling between beating flagella on motility [19–24]. However, there is growing evidence that such couplings are unlikely to play a significant role, especially in the case of biciliated organisms like *Chlamydomonas Reinhardtii* [25–27]. These studies indicate that their motility must arise from simple mechanical coupling between active components and the organism’s body. Previous research conducted on microorganisms strongly supports this notion [26, 28–30]. Thus, it remains to be seen whether an artificial model system that demonstrates and validates the emergence of RT motion based on these mechanisms can be envisaged.

In past, attempts have been made to mimic various dynamical features of microorganisms in synthetic systems [31–37]. Notwithstanding, an artificial analogue system that accurately mimics RT motion with quick, straight run trajectories and slow, sharp tumbles is lacking. While there are reports of RT-like motion in vibrated granular particles [38] and self-propelling camphor boats [39], these studies often feature long tumble durations and very short runs. This behavior contrasts with microorganisms, where runs typically last approximately an order of magnitude longer than tumbles [4–6]. This discrepancy likely originates from finite inertial effects in these mesoscale synthetic systems [40–43], limiting their relevance to microscopic organisms that exclusively operate in a low Reynolds number regime. Therefore, for a mesoscale artificial model system to accurately reproduce RT motion, it must similarly operate in an overdamped regime. To the best of our knowledge, no experimental system currently exists that fulfills these conditions while

* Equal contribution

† harsh@iitmandi.ac.in

‡ nkumar@iitb.ac.in

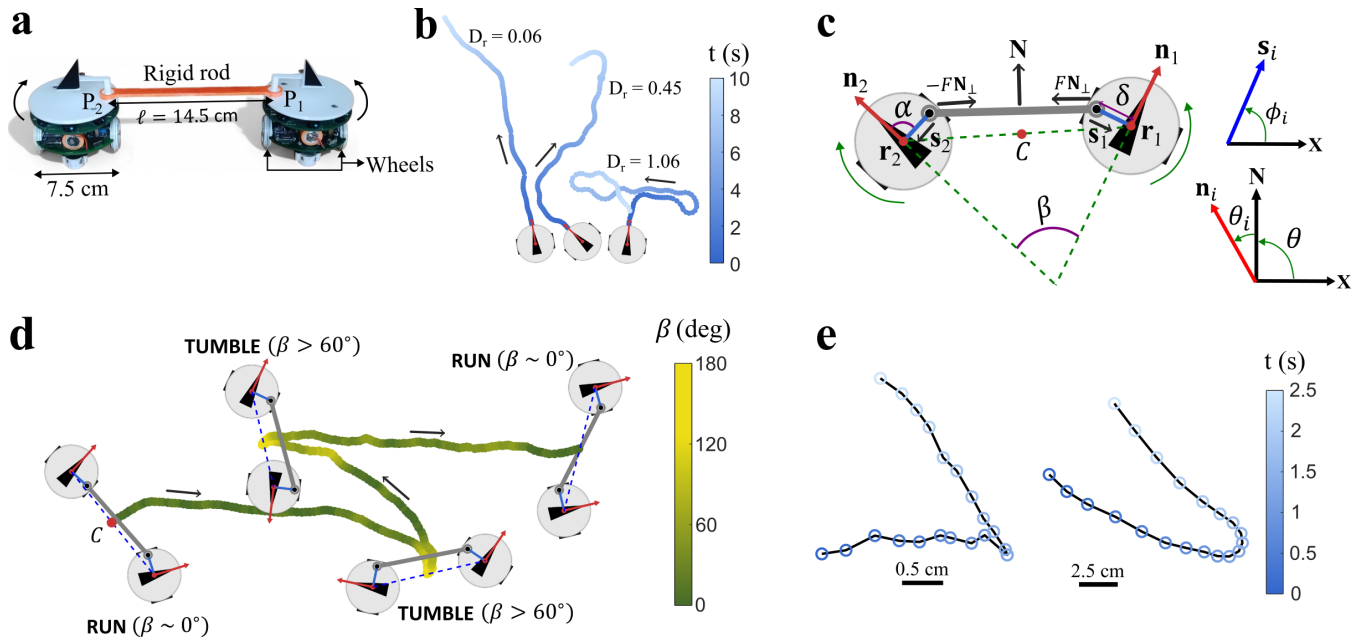


FIG. 1. **An analog robotic model system executing run-and-tumble (RT) motion:** (a) Photograph of the experimental system featuring two coupled robots. The pivot points, P_1 and P_2 , allow the connecting rod to rotate freely in the horizontal plane. (b) Each robot is programmed to perform overdamped active Brownian (AB) motion with a constant self-propulsion speed $v_a = 5 \text{ cm s}^{-1}$. Representative trajectories of the free robots are shown for three different values of the rotational diffusion constant, D_r (in $\text{rad}^2 \text{ s}^{-1}$). (c) Schematic diagram of the experimental setup, highlighting key variables incorporated into the theoretical model. (d) A typical RT trajectory of the centroid point C , for the coupled robot system with $v_a = 5 \text{ cm s}^{-1}$, $D_r = 0.06 \text{ rad}^2 \text{ s}^{-1}$, $\delta = 3 \text{ cm}$, and $\alpha = 90^\circ$. The color bar shows the value of the pair angle parameter β . Black arrows along the trajectory indicate the direction of motion. (e) Zoomed-in views of typical tumble events under conditions of high (left) and low (right) substrate friction. Low friction results in the wheel skidding, introducing significant inertial time delay and causing tumble events to vanish. We increased v_a to 20 cm s^{-1} for low friction case to better illustrate the effect.

providing tunable statistical features of the RT motion.

To this end, we introduce an experimental model system supported by a theoretical framework executing highly tunable RT-like dynamics. The setup is rather simple and involves two disk-shaped programmable, wheeled robots physically connected by a rigid rod. The connecting rod is free to rotate within the horizontal plane, with its ends pivoted at specific, mirror-symmetric points on each robot. The setup is conceived to model robots as active components and the rod as the body of an organism. The rod's placement on each robot is arbitrary, serving as an analogy for biochemical processes that internally regulate filamentary connections [28]. Due to their unique propulsion mechanism based upon rolling-without-slipping wheels, each robot executes an overdamped active Brownian (AB) motion at its center with negligible inertial effects. This AB motion is characterized by a propulsion speed v_a and rotational diffusion constant D_r which is programmed into each robot. The mechanical linkage transforms the active force exerted by each robot combined with its rotational diffusion into a stochastic torque around vertical axes passing through pivot points. This torque acts in opposite directions for two robots, resulting in the coupled system exhibiting self-actuated motion resembling RT dynamics. We characterize the motion using a single

parameter, the tumbling frequency, λ , and show that it can be systematically varied as a function of locations of linkage points. We also present a theoretical model that relies on Langevin dynamics for connected robots treated as overdamped AB particles. Our model also accounts for torques experienced by robots due to the connecting rod and successfully explains the experimental results, providing a deeper understanding of the origin of RT-like motility in microorganisms.

In this paper, we adopt an integrated experimental and theoretical approach, conducting simulations based on our theoretical model alongside the experiments. We use a consistent color scheme throughout: experimental results are shown in blue, and simulation in red whenever they are presented together. It is essential to clarify that we have kept our theoretical model minimal by ignoring detailed experimental features of the propulsion mechanism of the robots. Therefore, the goal of our theoretical model is not to achieve a quantitative match with experiments but to capture qualitative characteristics and general trends.

II. EXPERIMENTAL AND THEORETICAL MODEL

Our experimental system consists of two two-wheeled, self-propelled, programmable robots, described in our previous studies (Fig. 1(a), also Supplemental Material (SM) section IA) [44, 45]. Each robot is 7.5 cm in diameter and individually programmed to execute in-plane overdamped active Brownian (AB) motion along axes passing through their centers, aligned parallel to their wheels [44]. Both robots are equipped with 3D-printed caps featuring black, triangle-shaped markers, enabling precise tracking of their in-plane positions and orientations. The AB trajectories of the single, non-connected robot are shown in Fig. 1(b) for $v_a = 5 \text{ cm s}^{-1}$ and three typical values of D_r (see SM movie 1). Central to their overdamped property is the fact that they propel forward using their wheels, which roll without slipping on a flat glass surface covered with a white sheet of paper. This provides sufficient traction for the wheels, making the effects of inertia negligible. Next, we physically connected these robots with a rigid rod of length $\ell = 14.5 \text{ cm}$ (Fig. 1(a)). The rod is free to rotate about pivot points (P_1 and P_2) located on the left and right sides of the two robots, respectively. Here, we vary δ and α between 1 and 3 cm and 30° and 150° in intervals of 1 cm and 30° respectively. A combination of self-propulsion and constraint force due to the rigid rod generates net torque around vertical axes passing through P_1 and P_2 . These torques act in opposite handedness for the two robots indicated by curved arrows in Fig. 1(a).

Next, we develop a simplified model details of which are presented in the SM section IIA and IIB. Here, all dissipative forces, such as frictional and resistive, acting on a single robot with translational velocity \mathbf{v} and rotational velocity $\boldsymbol{\omega}$ are lumped into generalized expressions:

$$\mathbf{F}_d = -\boldsymbol{\Gamma} \cdot \mathbf{v}, \quad (1)$$

$$\boldsymbol{\tau}_d = -\Gamma_\tau \boldsymbol{\omega}, \quad (2)$$

where $\boldsymbol{\Gamma}$ and Γ_τ are the dissipation tensor and dissipation coefficient for translational and rotational motion, respectively. We assume that even when connected, robots continue to operate in an overdamped regime in experiments. We also ignore any dependence of $\boldsymbol{\Gamma}$ and Γ_τ on \mathbf{v} and $\boldsymbol{\omega}$ in the leading order. In experiments, the robot encounters significantly greater frictional forces perpendicular to its polar axis (due to wheel sliding) compared to those in the parallel direction (from rolling wheels). As a result, $\boldsymbol{\Gamma}$ assumes a non-scalar matrix form that depends on the robot's orientation \mathbf{n} . The dissipative forces along and perpendicular to \mathbf{n} are expressed as $-\Gamma_\parallel \mathbf{v}_\parallel$ and $-\Gamma_\perp \mathbf{v}_\perp$, respectively, where \mathbf{v}_\parallel and \mathbf{v}_\perp denote the projections of \mathbf{v} parallel and perpendicular to \mathbf{n} , and Γ_\parallel and Γ_\perp are positive constants.

Based on the above assumptions, our minimal model of the coupled AB robots, schematically sketched in Fig. 1(c), is as follows. Let \mathbf{n}_i ($i = 1 \& 2$ for two robots) represent the direction of the active velocity of the i th

robot, and \mathbf{s}_i denote the direction from the pivot point P_i to robot center \mathbf{r}_i . The equations of motion for the robot centers \mathbf{r}_i and orientation angles ϕ_i of \mathbf{s}_i read

$$\frac{d\mathbf{r}_i}{dt} = \mathbf{n}_i v_a + p_i F \left[\gamma \mathbf{n}_i (\mathbf{n}_i \cdot \mathbf{N}_\perp) + \frac{1}{\Gamma_\perp} \mathbf{N}_\perp \right], \quad (3a)$$

$$\frac{d\phi_i}{dt} = -p_i F \delta \frac{1}{\Gamma_\tau} \mathbf{s}_i \cdot \mathbf{N} + \sqrt{2D_r} \eta_i(t), \quad (3b)$$

where $\eta_i(t)$ is delta-correlated white Gaussian noise for the i th robot, with η_1 and η_2 being uncorrelated, and \mathbf{N} is the unit vector normal to the rod and \mathbf{N}_\perp is the unit vector along the rod (Fig. 1c). Here $p_1 = 1$, $p_2 = -1$ and $\gamma = (\Gamma_\perp - \Gamma_\parallel) / (\Gamma_\perp \Gamma_\parallel)$. The force F , calculated using the constraint that the distance between the P_1 and P_2 remains fixed to the rod length ℓ , is given by

$$F = \mathcal{G}(\theta_1, \theta_2) \left\{ -v_a L_\perp + \sqrt{2D_r} \delta [-\cos(\theta_1 + \alpha) \eta_1 + \cos(\theta_2 - \alpha) \eta_2] \right\} \quad (4)$$

where θ_i is the orientation angle of \mathbf{n}_i with respect to \mathbf{N} and it has the following relation with ϕ_i :

$$\phi_1 = \theta_1 + \theta + \alpha - \pi, \quad \phi_2 = \theta_2 + \theta + \pi - \alpha. \quad (5)$$

The function \mathcal{G} has the following form

$$\mathcal{G}(\theta_1, \theta_2) = \frac{1}{\gamma K_\perp + \frac{\delta^2}{\Gamma_\tau} M_\perp + \frac{2}{\Gamma_\perp}}. \quad (6)$$

The equation of motion for the orientation angle θ of \mathbf{N} , details of which are provided in SM section IIB, is given by

$$\frac{d\theta}{dt} = \frac{v_a}{\ell} L_\parallel + \frac{1}{\ell} \left(\gamma K_\parallel + \frac{\delta^2}{\Gamma_\tau} M_\parallel \right) F + \frac{\delta}{\ell} \sqrt{2D_r} [-\sin(\theta_1 + \alpha) \eta_1 + \sin(\theta_2 - \alpha) \eta_2]. \quad (7)$$

where K_\perp , M_\perp , L_\perp , K_\parallel , M_\parallel , and L_\parallel are functions of θ_1 and θ_2 . Their explicit forms are provided in Equations (32)-(37) in the SM section IIB.

By solving Eq. (7) for $\theta(t)$, we determine \mathbf{N} , which is then used in Eqs. (3) to compute the trajectories of \mathbf{r}_i and ϕ_i . Subsequently, we obtain the trajectory of the centroid of two robots $\mathbf{r} = (\mathbf{r}_1 + \mathbf{r}_2)/2$ indicated by point C . We set all parameters to the values used in the experiments, except for the following phenomenological ratios, which are adjusted to best match the experimental results: $\Gamma_\parallel/\Gamma_\perp = 0.1$ and $4\Gamma_\tau/(\Gamma_\parallel d^2) = 1$, where $d = 7.5 \text{ cm}$ is the diameter of our robots.

III. RESULTS

We start with parameters $\alpha = 90^\circ$ and $\delta = 3 \text{ cm}$. When connected robots are set in motion, their centroid, C , exhibits dynamics resembling fast, nearly straight trajectories (runs) with occurrences of abrupt sharp turns

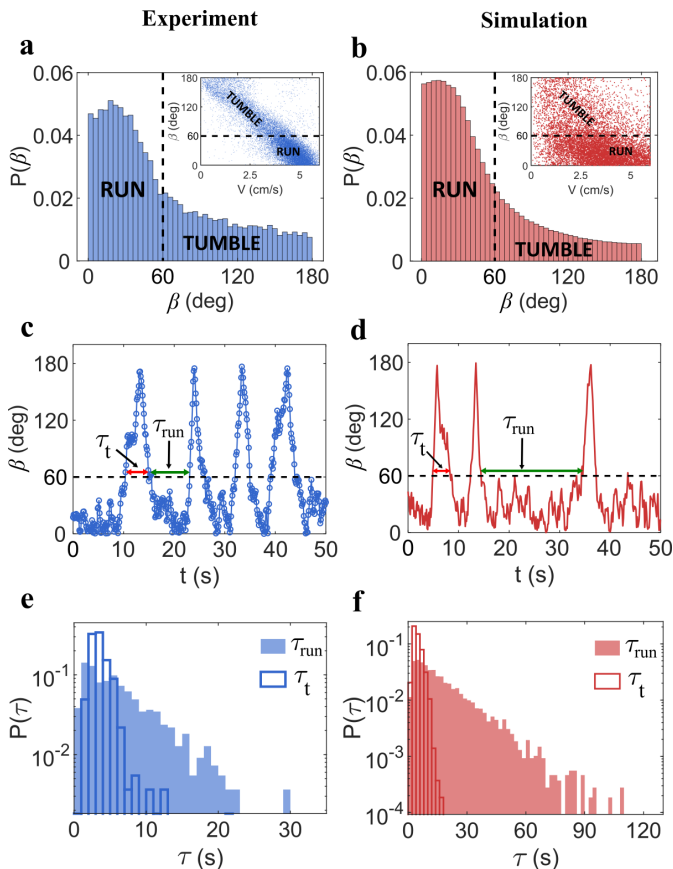


FIG. 2. Characterization of RT motion in experiment and simulation: (a, b) Probability distribution of β shows a pronounced peak near $\beta = 0^\circ$. Inset: small β values correspond to faster dynamics whereas higher values correspond to slow speeds. Black dashed lines at $\beta = 60^\circ$ set an arbitrary threshold to differentiate between run and tumble events. (c, d) The parameter β plotted as a function of time t . τ_t and τ_{run} represent tumble duration and run-time respectively. (e, f) In both experiment and simulation, we observe exponentially decaying run times and unimodal tumble durations. Experimental and simulation parameters are $v_a = 5 \text{ cm s}^{-1}$, $D_r = 0.06 \text{ rad}^2 \text{ s}^{-1}$, $\delta = 3 \text{ cm}$, and $\alpha = 90^\circ$.

and sudden halts (tumbles). A typical trajectory is shown in Fig. 1(d) and SM movie 2 for $D_r = 0.06 \text{ rad}^2 \text{ s}^{-1}$ and $1.33 \text{ rad}^2 \text{ s}^{-1}$ in SM movie 3. We reproduce these dynamics in simulations by numerically solving Eqs. (3) and (7) of our theoretical model (SM movies 2 and 3). As a vital point, we find it essential to minimize inertial time scales in capturing sudden, sharp tumbling events in experiments. This implies minimizing factors of m/Γ_{\parallel} , m/Γ_{\perp} and I/Γ_{τ} where m and I are the mass and the moment of inertia of each robot respectively (Eqs. 4 and 5 in SM section IIA). To achieve this limit, we performed an experiment on a slippery glass surface coated with coconut oil. Interestingly, we find that a majority of tumbling events become significantly smoother, making them harder to distinguish from run states (See Fig. 1(e) and SM movie 4). In contrast, such smooth turns are rare on

a frictional substrate. These findings are in accordance with previous studies in some active matter experiments where inertial effects are known to introduce time delays preventing abrupt changes in direction [40–42]. We further demonstrate that the RT motion does not occur when individual robots are programmed to perform Brownian dynamics (SM movie 5 and SM section ID), confirming its inherently active nature [46]. Henceforth, all experimental results are obtained from experiments conducted on a frictional surface.

To carry out statistical analysis of the resulting RT motion, we record long-time trajectories comprising hundreds of running and tumbling events for experiments and simulations. In experiments, we eliminate trajectories that experienced disruptions due to boundary walls (see SM section IC for more details). We find that two key parameters effectively describe the RT motion: the pair angle $\beta(t)$ representing the instantaneous difference in the in-plane orientations of two robots (see schematic Fig. 1(c)) and the instantaneous speed $V(t)$ of the centroid C . A typical distribution of β is shown in Figs. 2(a) and 2(b) for experiment and simulation, respectively. We also find that these parameters are inversely related to each other (inset of Figs. 2(a) and 2(b)) with a cluster of points at high-speed values corresponding to low values β , which we identify as run states. To differentiate runs from tumbles in a quantitative sense, we set an arbitrary threshold of $\beta = 60^\circ$, corresponding approximately to the half-maximum of the run peak. The typical behaviour of β as a function of time is shown in Figs. 2(c) and 2(d) for experiment and simulation, respectively. By using $\beta = 60^\circ$ as a reference line, we quantify both the tumbling duration (τ_t) and run-time (τ_{run}) from this time series for both experiment and simulation. The resulting distributions τ_{run} show exponential decay in each case (Figs. 2(e) and 2(f)). Encouragingly, such exponential decays are ubiquitous in many microorganisms like swimming bacteria [4], *Chlamydomonas Reinhardtii* algae [5], and amoeba [6]. Our experiments also reveal that tumbles are sudden events, with τ_t uniformly distributed around its mean value, which is approximately five times smaller than the average τ_{run} in experiments, consistent with observations made in real biological systems [4, 5].

Next, inspired by theoretical models used for modeling RT motion [47–52], we quantify this motion in terms of tumbling frequency, denoted by λ . Visual analysis of trajectories shows that a tumbling event happens when at least one robot undergoes a complete rotation (see SM movie 6). This is always accompanied by $\beta(t)$ peaking at 180° (Figs. 2(c) and 2(d) for experiment and simulation respectively). Using this criterion, we calculate λ as the mean time-frequency of occurrences of such tumble peaks. We find that for $\alpha = 90^\circ$, λ shows a systematic variation as a function of δ and D_r , as shown in Fig. 3(a) and 3(b) for experiment and simulation, respectively. Our results show that both δ and D_r promote tumbling in the system along the expected lines as they introduce stochasticity in the run state and increased

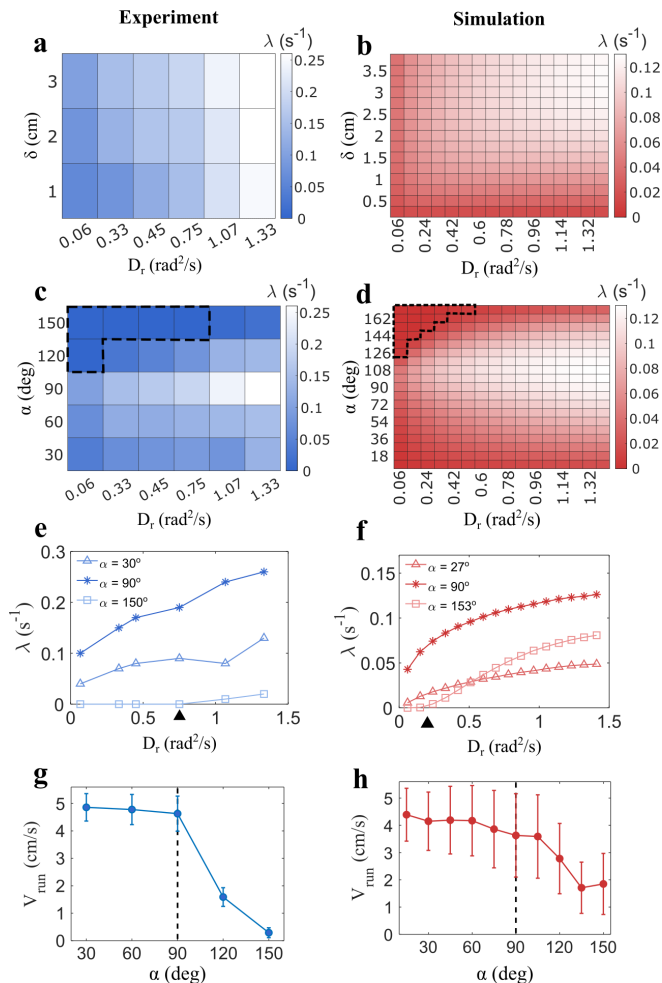


FIG. 3. **Quantifying RT motion in terms of tumbling frequency in experiment and simulation:** (a, b) The tumbling frequency, λ increases with higher D_r and δ . (c, d) The phase diagram of λ in $\alpha - D_r$ plane for $\delta = 3$ cm shows that run events become significantly more likely for $\alpha > 90^\circ$. The region enclosed by the dashed line corresponds to $\lambda \approx 0$. (e, f) λ exhibits a critical D_r indicated by a black arrowhead beyond which tumbling emerges in the system. (g, h) The run speed, $V_{\text{run}} \approx v_a$ for $\alpha \leq 90^\circ$ but decreases monotonically for $> 90^\circ$. Error bars represent standard deviation.

torque, respectively (Eq. (3b)). The system also shows interesting phase behaviour when we vary the parameter α . Experiments and simulation show that the run state becomes considerably stable for $\alpha > 90^\circ$. This is indicated by regions surrounded by dashed lines corresponding to vanishing λ in Fig. 3(c) and (d) for experiment and simulation, respectively. When we plot λ as a function of D_r for various values of α , we find a well-defined critical D_r beyond which λ increases abruptly indicated by black arrowheads in Figs. 3(e) and 3(f). On the contrary, for $\alpha \leq 90^\circ$, λ shows a gradual increase with D_r . We further observe that the mean run speed, V_{run} , calculated by taking the average of V while running, remains independent of α for $\alpha \leq 90^\circ$ and decreases with α as

exceeds 90° (Fig. 3(g) and (h) for experiment and theory respectively). In summary, our system provides various experimental parameters that can be adjusted to modify the tumbling frequency, emphasizing the importance of the physical coupling of active units in the propulsion mechanism.

Next, we develop a theoretical framework to explain the observed RT dynamics in our system and to provide a rationale for the $\alpha - D_r$ phase diagram. As observed in experiments and numerical simulations, the dynamics of the system at any given time are entirely governed by its internal configuration, which is represented by variables θ_i ($i = 1$ and 2 for two robots) (Fig. 4(a)). Therefore, we define another set of generalized angular coordinates: $\theta_\pm = (\theta_1 \pm \theta_2)/2$ (see Fig. 4(a)). Note that $\beta = |\theta_p|$, where θ_p is the principal value of the angle $2\theta_-$ in the range $[-\pi, \pi]$ and θ_+ indicates the average orientation of the robots with respect to the rod. Fig. 4(a) clearly shows that motility causes increasing and decreasing trends in θ_1 and θ_2 , respectively. Therefore, by definition, θ_- also increases with time over large time scales. Moreover, for integers n , when $\theta_- = n\pi$, the coupled robots move with the maximum possible speed of v_a . Similarly, when $\theta_- = (2n + 1)\pi/2$, the system shows tumbling behavior. To elaborate further, we derive the equations of motion for θ_\pm from Eqs. (3b) and (7), using the relation provided in Eq. (5), which are given as follows (also see SM section IIC):

$$\frac{d\theta_\pm}{dt} = \mathcal{T}_\pm + \sqrt{2D_\pm}\eta_\pm(t) \quad (8)$$

where

$$\mathcal{T}_+ = 2v_a \sin \theta_- \left(\frac{1}{\ell} \sin \theta_+ - \cos \theta_+ \mathcal{GH} \right) \quad (9)$$

$$\mathcal{T}_- = -\frac{2\delta v_a}{\Gamma_\tau} \mathcal{G} \cos^2 \theta_+ \cos(\theta_- + \alpha) \sin \theta_- \quad (10)$$

and D_\pm and \mathcal{H} are the functions θ_+ , θ_- , and α (see SM section IIC). The strengths of the noise terms D_\pm in Eq. (8) are of the order of D_r .

Let us now analyze the effect of the deterministic components \mathcal{T}_\pm on the dynamics of θ_\pm . In Figs. 4(b)-4(d), we display the flow profiles of the angular coordinates (θ_+, θ_-) in the absence of noise. The color map represents the magnitude \mathcal{T} in rad s^{-1} of the vector with two components $(\mathcal{T}_+, \mathcal{T}_-)$. Note that the system is invariant under the transformations $\theta_1 \rightarrow \theta_1 \pm 2\pi$ and $\theta_2 \rightarrow \theta_2 \pm 2\pi$. Consequently, it remains invariant under $(\theta_+, \theta_-) \rightarrow (\theta_+ \pm \pi, \theta_- \pm \pi)$ and $(\theta_+, \theta_-) \rightarrow (\theta_+ \pm \pi, \theta_- \mp \pi)$. This implies that the first and third quadrants, as well as the second and fourth, represent the same set of systems. This symmetry is evident in the flow profiles as well.

We begin with the case where $\alpha > 90^\circ$, with a typical flow profile shown for $\alpha = 120^\circ$ (Fig. 4(b)). Here, we find two stable and two unstable fixed points denoted by S_1, S_2 , and U_1, U_2 respectively. We also observe an unstable fixed line along $\theta_- = n\pi$ which is less relevant to

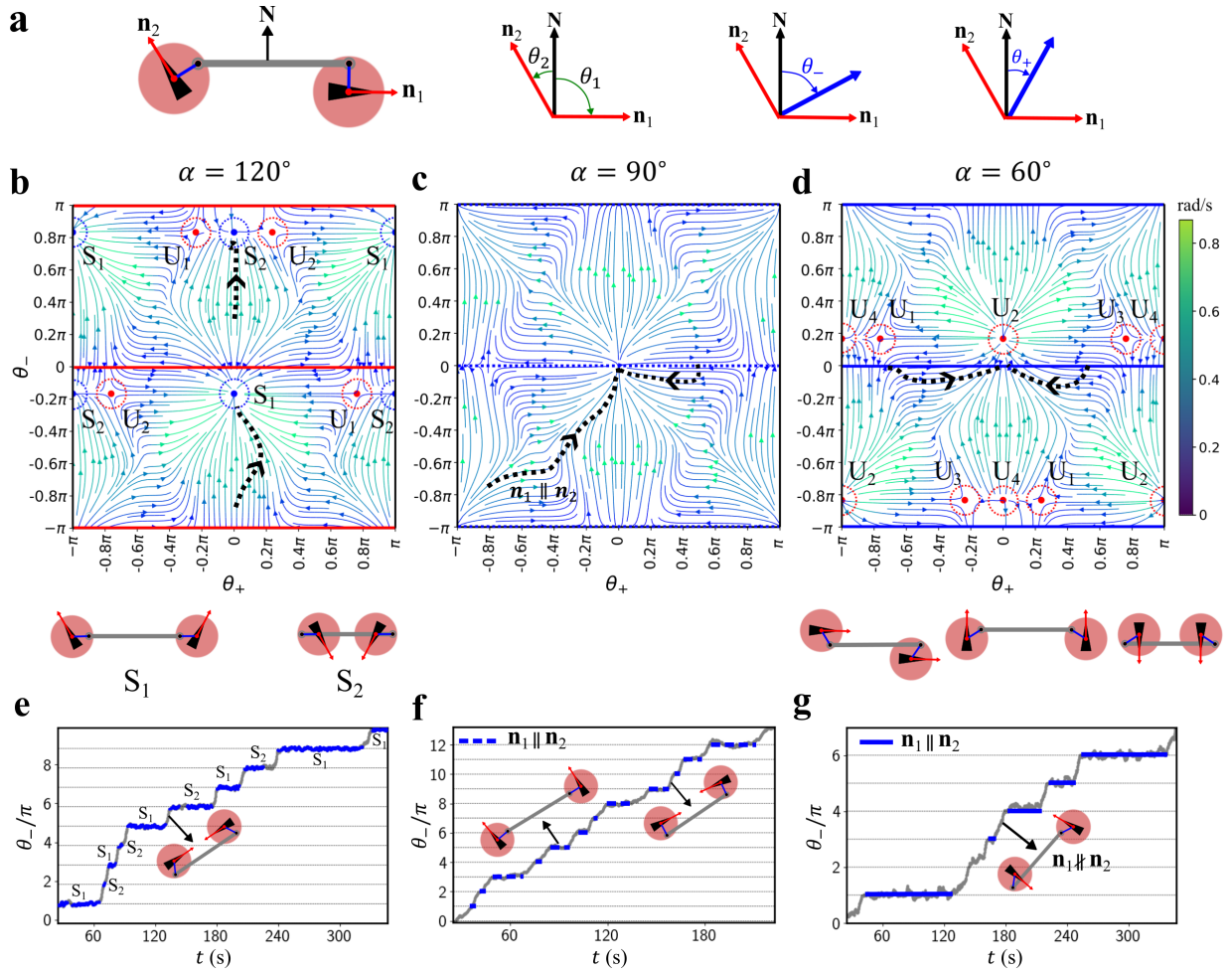


FIG. 4. **Understanding RT motion using flow-diagrams of angular coordinates (θ_+, θ_-) :** (a) A schematic diagram clarifying the angular coordinates (θ_+, θ_-) . Here, $\theta_{\pm} = (\theta_1 \pm \theta_2)/2$. (b) Flow diagram of (θ_+, θ_-) for $\alpha = 120^\circ$ evaluated from the deterministic part \mathcal{T}_{\pm} of Eq. (8). Blue circles around stable points S_1 and S_2 are regions where flow lines converge, representing the run states of the system. Red circles around unstable points U_1 and U_2 are regions of diverging flow lines. Experimental trajectories for $D_r = 0$ are illustrated as black dashed lines (see SM movie 7). Schematic configurations corresponding to S_1 and S_2 are shown at the bottom. \mathbf{n}_1 and \mathbf{n}_2 are misaligned by an angle of $2\alpha - \pi = 60^\circ$ in both cases. (c) Flow diagram for $\alpha = 90^\circ$. Blue dotted lines at $\theta_- = n\pi$ are semi-stable in θ_- and neutral in θ_+ , where n denotes positive integers. See SM movie 8 for the experimental trajectories of $D_r = 0$ in black dashed lines. (d) Flow profile for $\alpha = 60^\circ$. The system exhibits four unstable points (U_1, U_2, U_3 , and U_4). Solid blue lines at $\theta_- = n\pi$ represent configurations that are stable in θ_- and neutral in θ_+ . The black dashed experimental trajectories for the $D_r = 0$ case closely follow the stable lines (see SM movie 9). The system features infinitely many stable run configurations, corresponding to $\mathbf{n}_1 \parallel \mathbf{n}_2$, a few of which are shown at the bottom. The color bars in all these flow diagrams correspond to the magnitude of the vector $(\mathcal{T}_+, \mathcal{T}_-)$ in rad s^{-1} . (e), (f) & (g) show θ_- vs t obtained from the numerical solution of Eq. (8) for $\alpha = 120^\circ, 90^\circ$ and 60° , and $D_r = 0.06 \text{ rad}^2 \text{ s}^{-1}$. For $\alpha = 120^\circ$, the plateaus at $\theta_- = n\pi - \pi/6$ (indicated by dotted gray lines) correspond to run states near the stable states S_1 and S_2 . For $\alpha = 90^\circ$ and $\alpha = 60^\circ$, the plateaus occur at $\theta_- = n\pi$, corresponding to infinitely many run configurations with $\mathbf{n}_1 \parallel \mathbf{n}_2$. Switches between these states occur through configurations where $\mathbf{n}_1 \not\parallel \mathbf{n}_2$.

the results presented. Locations of stable points in the first and second quadrants are $(\theta_+, \theta_-) = (\pi, 3\pi/2 - \alpha)$ and $(0, 3\pi/2 - \alpha)$ for S_1 and S_2 respectively, with system configurations shown below Fig. 4(b). Clearly, both configurations lead to a run state. Interestingly, in this case, the stable run states do not correspond to aligned robots (as was the case for $\alpha = 90^\circ$), but rather to anti-aligned vectors \mathbf{s}_i . Here, the system favors these stable points for low noise values, resulting in a pronounced run regime at

low D_r values, as shown in Figs. 3(e) and 3(f). To test this, we conducted experiments for the $D_r = 0$ case using random initial conditions in (θ_+, θ_-) and observed that the system follows the predicted flow lines (black dashed lines in Fig. 4(b)) before eventually settling into one of the stable regions, indicated by the dashed circular regions (see SM movie 7). Moreover, as evident from configurations S_1 & S_2 , the system's run speed at the stable points is given by $v_a \sin \alpha$, which decreases

with α for $\alpha > 90^\circ$. This explains the decreasing trend in V_{run} shown in Figs. 3(g) and 3(h).

An alternate way to visualize RT dynamics is through the time dependence of the parameter θ_- . In Fig. 4(e), which corresponds to $D_r = 0.06 \text{ rad}^2 \text{ s}^{-1}$ in simulation, we find that θ_- always plateaus around $\pi/2 - \alpha + n\pi$, which equals $\theta_- = n\pi - \pi/6$ for $\alpha = 120^\circ$ shown by gray dotted lines. However, due to rotational noise, the system occasionally escapes its stable points, causing it to jump between stable states by a value of π leading to a tumbling event. As D_r increases, the system is more likely to escape the stable points sooner, leading to an increased tumbling rate, as observed in both simulations and experiments.

For $\alpha = 90^\circ$, no stable fixed points are observed. Instead, there exists a fixed line at $\theta_- = n\pi$, which is semi-stable in θ_- and neutral in θ_+ (blue dashed line in Fig. 4(c)). Therefore, as the system reaches this line, it runs for a while, before sliding towards increasing θ_- due to noise. Experiments performed at $D_r = 0$, in this case, show traced paths that agree well with theoretical values (see SM movie 8). Also, as shown in Fig. 4(f), the system still tends to stay closer to $\theta_- = n\pi$ (dotted gray lines) due to the neutral nature, although only for a short period, describing the origin of RT dynamics on our system for $\alpha = 90^\circ$ shown in Fig. 1.

Finally, for $\alpha < 90^\circ$, and using $\alpha = 60^\circ$ as a typical example, we find four unstable points and a fixed line at $\theta_- = n\pi$ as shown in Fig. 4(d). This fixed line corresponds to infinitely possible configurations where robots are aligned (i.e., \mathbf{n}_i are parallel to each other with three typical ones schematically shown below Fig. 4(d)). Consequently, the system favors configurations along this line leading to run states with $V_{\text{run}} \approx v_a$ (as observed experimentally in Fig. 3(g)) that become progressively noisier with increasing D_r . Again, gray dashed line indicates the experimental trajectory for $D_r = 0$ case (SM movie 9). Furthermore, in Fig. 4(g), we present θ_- as a function of time, which exhibits relatively noisier plateaus corresponding to run states with occasional escapes, equivalent to the behavior observed for $\alpha > 90^\circ$. A key distinction, however, is that while the system for $\alpha > 90^\circ$ is limited to two stable run states, an infinite number of run configurations are possible when $\alpha < 90^\circ$.

Therefore, our theoretical model not only explains the emergence of complex RT motion in experiments but also elucidates how this complex behavior systematically depends on experimental parameters α and D_r .

IV. CONCLUSION AND DISCUSSION

Inspired by microorganism motility, we present a robotic model system that replicates run-and-tumble-like (RT-like) motion. Our minimal experimental setup consists of two self-propelled robots connected by a rigid rod, each exhibiting an overdamped active Brownian (AB) motion despite its mesoscopic, centimeter-scale size. The

rigid rod, attached to a pivot point on the robot's body, rotates freely and facilitates rotational motion. By varying the pivot placement relative to the robot's polarity axis, we observe a range of rich, tunable RT-like dynamics. We quantify the RT-like motion using the tumbling frequency and identify two key tuning parameters. The first, δ , is the distance of the pivot from the polarity axis, which promotes tumbling frequency by amplifying torque. The second, α , is the angle between the pivot-to-center line and the polarity axis, which also adjusts the tumbling frequency based on rotational noise programmed inside each robot. The tunability of RT motion with these parameters highlights the critical role of inter-flagella coupling through the organism's body in achieving synchronization cycles. We also developed a theoretical model that captures the essential features of our system and reproduces the experimental results, elucidating the intricate dependence of RT dynamics on δ and α .

A distinctive feature of our synthetic system is its ability to mimic overdamped dynamics, a hallmark of microorganisms operating at extremely low Reynolds numbers. Our robots, driven by motorized wheels through mechanical gears and responding to microcontroller signals, undergo rolling-without-slipping motion, thus faithfully emulating overdamped active Brownian motion. We also demonstrate that reducing wheel traction on the substrate by applying oil alters the tumbling event, causing it to lose its characteristic sharp and sudden turns. Moreover, simulation results by numerically solving the theoretical model, which also assumes overdamped rotational and translational dynamics, align well with experimental observations. These results suggest that similar design principles may underlie motility in microscopic organisms.

While our theoretical model qualitatively matches experimental results, it underestimates the tumbling frequency. This might be because of multiple intricate factors in our experimental system. For example, our theoretical model features propulsion force acting along an axis passing through the centre of the robot. Clearly, it ignores the fact that robots are driven through their wheels, and thus, propulsion forces act along two axes passing parallel to them. Additionally, weight distribution and the elevated placement of pivot points introduce additional torques and frictional differences between the wheels, factors omitted in our minimal model. Nevertheless, our theoretical framework uses the general AB model without such complications and, therefore, should capture the essential physics of overdamped dynamics in both living and artificial systems at microscopic scales. Our results thus provide a fundamental understanding of RT-like motion with broad implications for studying motility in active and living systems operating in low Reynolds number regimes.

ACKNOWLEDGEMENTS

NK acknowledges financial support from DST-SERB for CRG grant number CRG/2020/002925 and IITB for the seed grant. HS acknowledges SERB for the SRG (grant no. SRG/2022/000061-G). SP thanks CSIR India for the research fellowship (File no: 09/087(1040)/2020-EMR-I).

AUTHOR CONTRIBUTION STATEMENT

NK and HS designed the research. SP performed the experiments and analyzed data. UP and HS developed the theoretical model and ran simulations. All authors contributed equally in writing the paper.

-
- [1] S. Ramaswamy, The mechanics and statistics of active matter, *Annu. Rev. Condens. Matter Phys.* **1**, 323 (2010).
- [2] G. Gompper, C. Bechinger, H. Stark, and R. G. Winkler, Motile active matter, *The European Physical Journal E* **44**, 103 (2021).
- [3] H. C. Berg, Motile behavior of bacteria, *Physics today* **53**, 24 (2000).
- [4] H. C. Berg and D. A. Brown, Chemotaxis in escherichia coli analysed by three-dimensional tracking, *Nature* **239**, 500 (1972).
- [5] M. Polin, I. Tuval, K. Drescher, J. P. Gollub, and R. E. Goldstein, Chlamydomonas swims with two “gears” in a eukaryotic version of run-and-tumble locomotion, *Science* **325**, 487 (2009).
- [6] L. Li, S. F. Nørrelykke, and E. C. Cox, Persistent cell motion in the absence of external signals: a search strategy for eukaryotic cells, *PLoS one* **3**, e2093 (2008).
- [7] R. C. Findlay, M. Osman, K. A. Spence, P. M. Kaye, P. B. Walrad, and L. G. Wilson, High-speed, three-dimensional imaging reveals chemotactic behaviour specific to human-infective leishmania parasites, *Elife* **10**, e65051 (2021).
- [8] E. M. Purcell, Life at low reynolds number, in *Physics and our world: reissue of the proceedings of a symposium in honor of Victor F Weisskopf* (World Scientific, 2014) pp. 47–67.
- [9] H. C. Berg, Chemotaxis in bacteria., Annual review of biophysics and bioengineering **4**, 119 (1975).
- [10] M. Sidortsov, Y. Morgenstern, and A. Be’Er, Role of tumbling in bacterial swarming, *Physical Review E* **96**, 022407 (2017).
- [11] E. Lauga and R. E. Goldstein, Dance of the microswimmers, *Physics Today* **65**, 30 (2012), https://pubs.aip.org/physicstoday/article-pdf/65/9/30/10096373/30_1_online.pdf.
- [12] R. E. Goldstein, M. Polin, and I. Tuval, Emergence of synchronized beating during the regrowth of eukaryotic flagella, *Physical Review Letters* **107**, 148103 (2011).
- [13] D. R. Brumley, K. Y. Wan, M. Polin, and R. E. Goldstein, Flagellar synchronization through direct hydrodynamic interactions, *elife* **3**, e02750 (2014).
- [14] K. Y. Wan, K. C. Leptos, and R. E. Goldstein, Lag, lock, sync, slip: the many ‘phases’ of coupled flagella, *Journal of the Royal Society Interface* **11**, 20131160 (2014).
- [15] R. E. Goldstein, M. Polin, and I. Tuval, Noise and synchronization in pairs of beating eukaryotic flagella, *Physical review letters* **103**, 168103 (2009).
- [16] D. M. Woolley, R. F. Crockett, W. D. Groom, and S. G. Revell, A study of synchronisation between the flagella of bull spermatozoa, with related observations, *Journal of Experimental Biology* **212**, 2215 (2009).
- [17] D. Mondal, R. Adhikari, and P. Sharma, Internal friction controls active ciliary oscillations near the instability threshold, *Science advances* **6**, eabb0503 (2020).
- [18] B. M. Friedrich and F. Jülicher, Flagellar synchronization independent of hydrodynamic interactions, *Physical Review Letters* **109**, 138102 (2012).
- [19] R. R. Bennett and R. Golestanian, Emergent run-and-tumble behavior in a simple model of chlamydomonas with intrinsic noise, *Phys. Rev. Lett.* **110**, 148102 (2013).
- [20] M. Kim and T. R. Powers, Hydrodynamic interactions between rotating helices, *Phys. Rev. E* **69**, 061910 (2004).
- [21] A. Vilfan and F. Jülicher, Hydrodynamic flow patterns and synchronization of beating cilia, *Phys. Rev. Lett.* **96**, 058102 (2006).
- [22] T. Niedermayer, B. Eckhardt, and P. Lenz, Synchronization, phase locking, and metachronal wave formation in ciliary chains, *Chaos: An Interdisciplinary Journal of Nonlinear Science* **18**, 037128 (2008), https://pubs.aip.org/aip/cha/article-pdf/doi/10.1063/1.2956984/13860350/037128_1_online.pdf.
- [23] N. Uchida and R. Golestanian, Generic conditions for hydrodynamic synchronization, *Phys. Rev. Lett.* **106**, 058104 (2011).
- [24] N. Oliver, C. Alpmann, Á. Barroso, L. Dewenter, M. Werdemann, and C. Denz, Synchronization in pairs of rotating active biomotors, *Soft Matter* **14**, 3073 (2018).
- [25] B. M. Friedrich and F. Jülicher, Flagellar synchronization independent of hydrodynamic interactions, *Phys. Rev. Lett.* **109**, 138102 (2012).
- [26] G. Quaranta, M.-E. Aubin-Tam, and D. Tam, Hydrodynamics versus intracellular coupling in the synchronization of eukaryotic flagella, *Physical review letters* **115**, 238101 (2015).
- [27] G. S. Klindt, C. Ruloff, C. Wagner, and B. M. Friedrich, Load response of the flagellar beat, *Phys. Rev. Lett.* **117**, 258101 (2016).
- [28] K. Y. Wan and R. E. Goldstein, Coordinated beating of algal flagella is mediated by basal coupling, *Proceedings of the National Academy of Sciences* **113**, E2784 (2016).
- [29] V. F. Geyer, F. Jülicher, J. Howard, and B. M. Friedrich, Cell-body rocking is a dominant mechanism for flagellar synchronization in a swimming alga, *Proceedings of the National Academy of Sciences* **110**, 18058 (2013).
- [30] A. W. Soh, L. G. Woodhams, A. D. Junker, C. M. Enloe, B. E. Noren, A. Harned, C. J. Westlake, K. Narayan, J. S. Oakey, P. V. Bayly, *et al.*, Intracellular connections between basal bodies promote the coordinated behavior of motile cilia, *Molecular biology of the cell* **33**, br18 (2022).

- [31] Y. Xia, Z. Hu, D. Wei, K. Chen, Y. Peng, and M. Yang, Biomimetic synchronization in biciliated robots, *Physical Review Letters* **133**, 048302 (2024).
- [32] T.-l. Xu, C.-r. Qin, B. Tang, J.-c. Gao, J. Zhou, K. Chen, T. H. Zhang, and W.-d. Tian, Constrained motion of self-propelling eccentric disks linked by a spring, *The Journal of Chemical Physics* **161** (2024).
- [33] T. Sanchez, D. Welch, D. Nicastro, and Z. Dogic, Cilia-like beating of active microtubule bundles, *Science* **333**, 456 (2011).
- [34] I. Tiwari, P. Parmananda, and R. Chelakkot, Periodic oscillations in a string of camphor infused disks, *Soft Matter* **16**, 10334 (2020).
- [35] E. Han, L. Zhu, J. W. Shaevitz, and H. A. Stone, Low-reynolds-number, biflagellated quinke swimmers with multiple forms of motion, *Proceedings of the National Academy of Sciences* **118**, e2022000118 (2021).
- [36] P. Baconnier, D. Shohat, C. H. López, C. Coulais, V. Démercy, G. Düring, and O. Dauchot, Selective and collective actuation in active solids, *Nature Physics* **18**, 1234 (2022).
- [37] C. Hernández-López, P. Baconnier, C. Coulais, O. Dauchot, and G. Düring, Model of active solids: Rigid body motion and shape-changing mechanisms, *Phys. Rev. Lett.* **132**, 238303 (2024).
- [38] N. Kumar, R. K. Gupta, H. Soni, S. Ramaswamy, and A. Sood, Trapping and sorting active particles: Motility-induced condensation and smectic defects, *Physical Review E* **99**, 032605 (2019).
- [39] P. Dey, A. Thakur, A. Chotalia, A. Nandi, and P. Parmananda, Run-and-tumble-like motion of a camphor-infused marangoni swimmer, Not yet published (2025).
- [40] C. Scholz, S. Jahanshahi, A. Ldov, and H. Löwen, Inertial delay of self-propelled particles, *Nature communications* **9**, 5156 (2018).
- [41] D. Dutta, A. Kundu, and U. Basu, Inertial dynamics of run-and-tumble particle, arXiv preprint arXiv:2411.19186 (2024).
- [42] L. Caprini and U. Marini Bettolo Marconi, Inertial self-propelled particles, *The Journal of Chemical Physics* **154** (2021).
- [43] J. Fersula, N. Bredeche, and O. Dauchot, Self-aligning active agents with inertia and active torque, *Physical Review E* **110**, 014606 (2024).
- [44] S. Paramanick, A. Pal, H. Soni, and N. Kumar, Programming tunable active dynamics in a self-propelled robot, *The European Physical Journal E* **47**, 34 (2024).
- [45] S. Paramanick, A. Biswas, H. Soni, A. Pal, and N. Kumar, Uncovering universal characteristics of homing paths using foraging robots, *PRX Life* **2**, 033007 (2024).
- [46] A. Maitra, Activity unmasks chirality in liquid-crystalline matter, *Annual Review of Condensed Matter Physics* **16** (2024).
- [47] J. Tailleur and M. E. Cates, Statistical mechanics of interacting run-and-tumble bacteria, *Physical review letters* **100**, 218103 (2008).
- [48] R. W. Nash, R. Adhikari, J. Tailleur, and M. E. Cates, Run-and-tumble particles with hydrodynamics: Sedimentation, trapping, and upstream swimming, *Phys. Rev. Lett.* **104**, 258101 (2010).
- [49] M. E. Cates and J. Tailleur, When are active brownian particles and run-and-tumble particles equivalent? consequences for motility-induced phase separation, *Europhysics Letters* **101**, 20010 (2013).
- [50] E. J. Marsden, C. Valeriani, I. Sullivan, M. Cates, and D. Marenduzzo, Chemotactic clusters in confined run-and-tumble bacteria: a numerical investigation, *Soft Matter* **10**, 157 (2014).
- [51] A. P. Solon, M. E. Cates, and J. Tailleur, Active brownian particles and run-and-tumble particles: A comparative study, *The European Physical Journal Special Topics* **224**, 1231 (2015).
- [52] M. E. Cates and J. Tailleur, Motility-induced phase separation, *Annu. Rev. Condens. Matter Phys.* **6**, 219 (2015).